International Journal of Adhesion & Adhesives 116 (2022) 103148

Contents lists available at ScienceDirect

International Journal of Adhesion and Adhesives

journal homepage: www.elsevier.com/locate/ijadhadh

# Cohesive failure verification and fracture origin identification when the adhesive strength is expressed as a constant ISSF

Rei Takaki [a], Nao-Aki Noda [a,*], Yasuaki Suzuki [b], Yoshikazu Sano [a], Ko Hirata [a], Fuma Ito [a]

[a] Department of Mechanical Engineering, Kyushu Institute of Technology, 1-1 Sensui-cho, Tobata-ku, Kitakyushu-shi, Fukuoka, 804-8550, Japan
[b] Suzuki Adhesion Institute of Technology, 131 Aza-yashiki, Ukino, Chiaki-cho, Ichinomiya-shi, Aichi, 491-0806, Japan

ARTICLE INFO

*Keywords:*
Adhesion
Debonding strength
Intensity of Singular Stress Field (ISSF)
Cohesive fracture
Scarf joint
Fracture origin

ABSTRACT

The aim of this paper is to explain that the ISSF evaluation method can apply when the fracture is cohesive as well as an interface fracture. The cohesive fracture usually occurs very close to the adhesive joint's interface controlled by the intensity of singular stress field (ISSF). This is the reason why the adhesive strength can be evaluated as a constant value of ISSF. In this study, the fracture origin is confirmed at the interface end to verify the ISSF evaluation method. Next, the cohesive fracture near the interface is confirmed since the slight amount of adhesive remains near the polished streaks of the adherend steel. Finally, it is found that the cohesive fracture very close to the interface guarantees the appropriate adhesive strength which can be expressed as a constant value of the ISSF.

## 1. Introduction

Adhesive joining is widely used in many industrial fields such as automotive and aerospace industries, biomedical applications, and microelectronics [1–4]. Due to the increasing demand for joining dissimilar structural components, adhesive joining is gaining more and more interest because of light weight, low price, and high productivity [5–7]. For example, to support high-speed transmission signals and miniaturization and thinning in memory applications, semiconductor packaging technology has diversified structures towards including many interfaces composed of different materials, such as connection between semiconductors and substrates, encapsulation with resin, and multi-layered structure of semiconductor chips and wiring. When the number of dissimilar interfaces increases in this way, a singular stress field due to deformation mismatch is formed at each interface end, and the risk of peeling fracture increases. In the previous papers [7–10], the authors have shown that most of the adhesive joint strength can be expressed as a constant value of ISSF (Intensity of Singular Stress Field).

Regarding adhesive joints in general, it is known that cohesive fracture is stronger than interface fracture [11–13]. For example, Japanese automobile standards [11] prescribes that the adhesive design, adhesive process and the selection of adhesives should be reconsidered if the interface fracture is observed. This is based on the following reason. The adhesive bulk strength is based on the chemical bond (covalent bond) in the adhesive molecule. On the other hand, the debonding strength is based on the hydrogen bond of epoxy resin, polyurethane resin, etc. between the adherend and the adhesive or the van der Waals force. Suzuki [14] explained that compared to the chemical bond (covalent bond) energy controlling the adhesive strength, the hydrogen bond energy mainly controlling the adhesive strength is about 1/10 $(\mathrm{kJ\cdot mol^{-1}})/(\mathrm{kJ\cdot mol^{-1}})$, and the energy of the van der Waals force is about 1/100 $(\mathrm{kJ\cdot mol^{-1}})/(\mathrm{kJ\cdot mol^{-1}})$. Therefore, if the bonding surface is completely flat to the molecular level, the adhesive joint fracture is always interface fracture. In order to cause cohesive fracture, therefore, it is necessary to perform surface treatment such as sanding on the bonded surface to increase the actual surface area and generate the anchor effect. If such appropriate surface treatments are applied, the fracture can be 100% cohesive fracture.

Since the ISSF evaluation method is based on the singular stress field along the interface, many people may misunderstand that the interface fracture occurs when the adhesive strength is expressed as a constant value of the ISSF. In this paper, first, the fracture origin will be identified to confirm the validity of the ISSF evaluation method focusing on the scarf joints as well as the butt joint. Note that most of previous adhesive fracture observations were conducted without ISSF analysis results. Next, the fractured surface will be examined to confirm the fracture is cohesive or not especially focusing the fracture origin identified from the ISSF analysis. Finally, why the ISSF evaluation method is useful for

* Corresponding author.
*E-mail address:* noda.naoaki844@mail.kyutech.jp (N.-A. Noda).

https://doi.org/10.1016/j.ijadhadh.2022.103148

Available online 22 March 2022

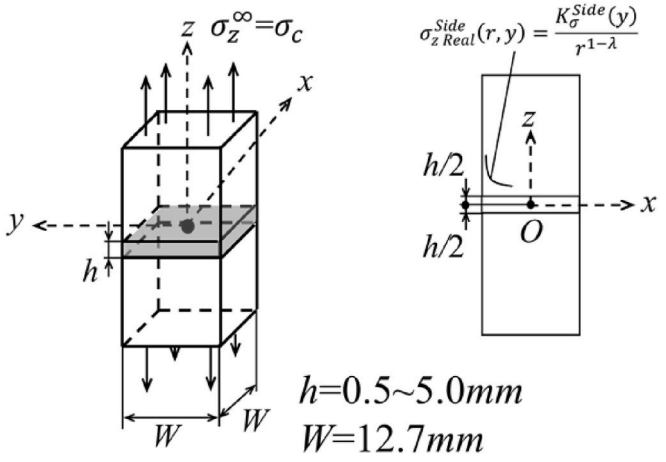


**Fig. 1.** Prismatic butt joint.

cohesive fracture will be clarified from the ISSF. The aim of this paper is to show that the ISSF evaluation method can apply when the fracture is cohesive as well as an interface fracture.

## 2. ISSF method to evaluate the adhesive strength

### *2.1. Adhesive strength expressed as a constant ISSF obtained from 2D analysis*

The ISSF calculation method was originally proposed by applying to the butt joint by using the mesh-independent technique named proportional method [8]. In the paper, the scarf joint is mainly focused. The prismatic butt joint in Fig. 1 can be regarded as a scarf joint whose scarf angle is 90°. The previous study [10] showed that the ISSF (Intensity of the singular stress field) along the adhesive interface edge ISSF ($K_{\sigma}(y)$) can be defined the real stress $\sigma_{z\,Real}$. Here, the term "real stress $\sigma_{z\,Real}$" is used to distinguish from the "FEM stress $\sigma_{z\,FEM}$" obtained from FEM analysis including some error.

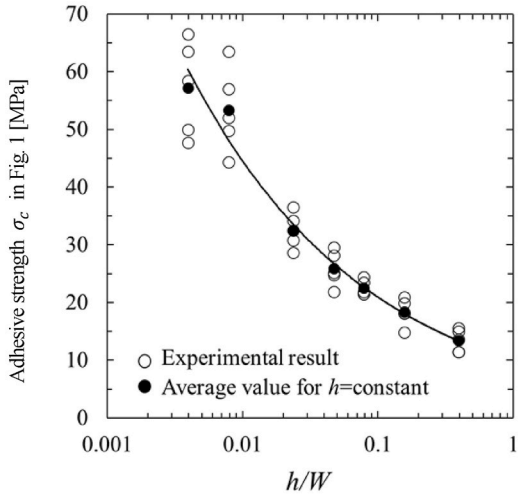


(a) Critical remote tensile stress $\sigma_c$ for Steel/ /Resin A

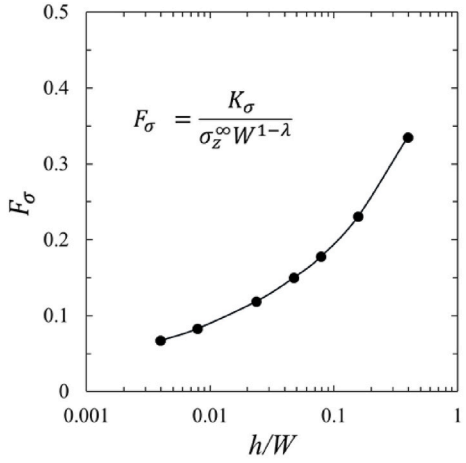


(b) Dimensionless ISSF $F_{\sigma}$ for Steel/ /Resin A obtained by 2D modelling

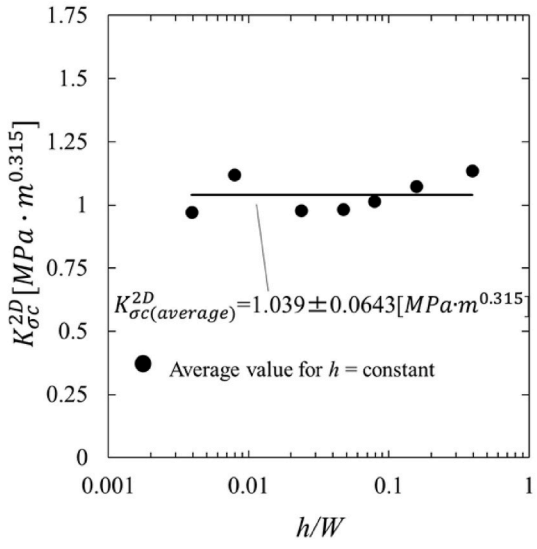


(c) Critical ISSF for Steel/ /Resin A

**Fig. 2.** Debonding strength for Steel//Resin A.

**Table 1**
Material properties for Steel/Epoxy Resin A [18,19].

| Material | | Young's modulus $E$ [GPa] | Poisson's ratio $\nu$ | Bulk strength $\sigma_B$ [MPa] | $\alpha$ | $\beta$ | Butt joint | Scarf joint | |
|---|---|---|---|---|---|---|---|---|---|
| | | | | | | | $\lambda$ | $\lambda_1$ | $\lambda_2$ |
| Adherend | S35C | 206 | 0.30 | 570 | 0.969 | 0.199 | 0.685 | 0.737 | 0.977 |
| Adhesive | Epoxy resin A | 3.14 | 0.37 | 65.5 | | | | | |

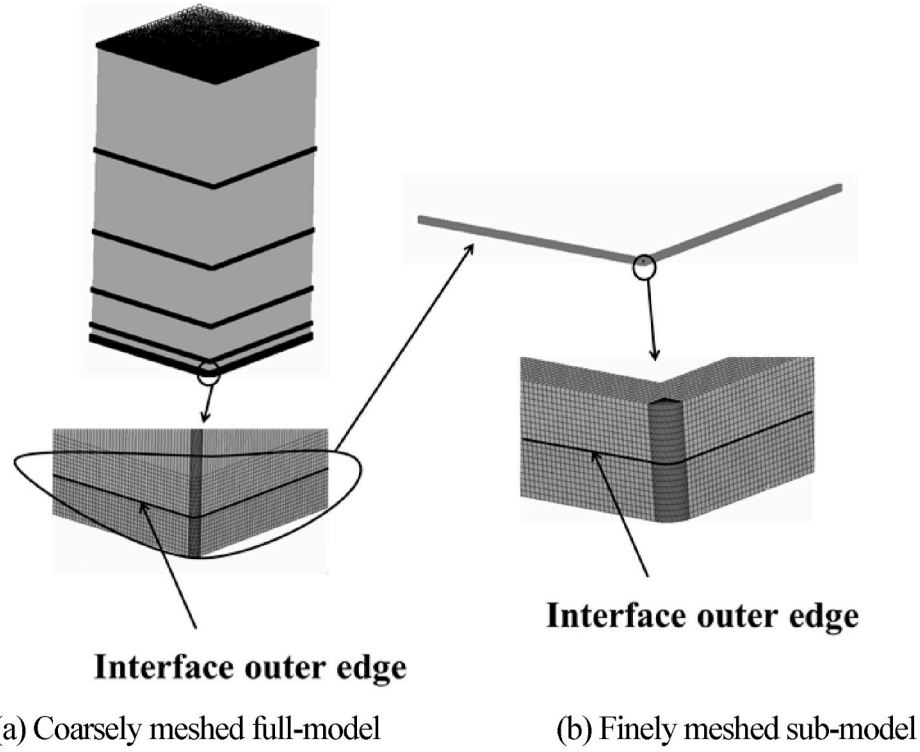


**Fig. 3.** FEM analysis modelling.

$$K_\sigma(y) = \lim_{r\to 0}\left[r^{1-\lambda} \times \sigma_{z\,Real}(r, y)\right] \tag{1}$$

Here, $\sigma_{z\,Real}(r, y)$ is the real stress appearing at the bonding interface, which can be represented by $\sigma_{z\,Real}(r, y) = K_\sigma(y)/r^{1-\lambda}$. The normalized ISSFs $F_\sigma(y)$ can be expressed by Eq. (2).

$$F_\sigma = \frac{K_\sigma}{\sigma_z^\infty W^{1-\lambda}} \tag{2}$$

Here, $\sigma_z^\infty$ denotes the remote tensile stress as shown in Fig. 1. In Eqs. (1) and (2), $\lambda$ is a singular index, which can be obtained from the eigen equation described in Section 2.2. Fig. 2(a) shows that the critical remote tensile stresses $\sigma_c$ increases with decreasing the bondline thickness $h$. The solid black circle denotes the average value obtained from 5 experimental results under $h$ = const. Fig. 2(b) indicates the normalized ISSF obtained by using the plane strain modelling [8–10]. From Fig. 2 (a), (b), the critical ISSF can be calculated as shown in Fig. 2(c) when the debonding occurs. The ISSF method may express the average adhesive strength within 7% error.

Table 1 shows the mechanical properties of the adherend and the adhesive Resin A with Dundurs parameter $\alpha$, $\beta$ and singularity index $\lambda$ [15,16]. Here, $\alpha$, $\beta$ are Dundurs parameters [15,16] defined from

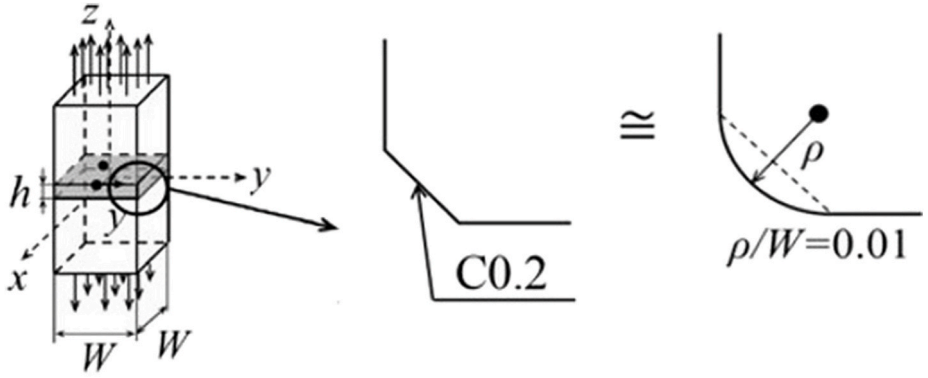


**Fig. 4.** Prismatic butt joint geometry with fillet.

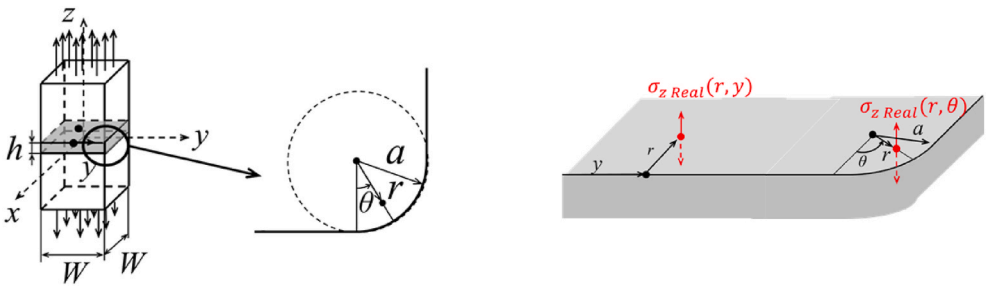


**Fig. 5.** Prismatic butt joint model with fillet considered in this study.

Poisson's ratio $\nu_j$ and shear modulus $G_j$ of the adherend and adhesive ($j = 1$ for the adherend, $j = 2$ for the adhesive). It is known that when $\alpha$ ($\alpha$-2$\beta$) $> 0$ the real stress $\sigma_{z\,Real}$ has a singularity of the form $\sigma_{z\,Real} \propto 1/r^{1-\lambda}$ ($\lambda < 1$).

### 2.2. Three-dimensional analysis to obtain the ISSF variation

In this section, how to obtain the ISSF variation is briefly explained in the three-dimensional prismatic butt joint by using the proportional method [8–10]. The same FEM mesh pattern is applied to the reference and unknown problems [8–10] since the FEM mesh error is almost the same when the mesh size is specified. Fig. 3 illustrates FEM model for one-eighth region of the prismatic butt joint in Fig. 1 assuming the corner fillet radius $\rho$. From the symmetry, at $z = 0$ in Fig. 1, the boundary conditions $u_x = 0$ at $x = 0$, $u_y = 0$ at $y = 0$ and $u_z = 0$ can be applied. Fig. 4 shows the butt joint geometry near the corner. By considering the real chamfer dimension [17] in Fig. 4, $\rho = 0.0127$ mm ($\rho/W = 0.01$) is focused. By considering the experiment [18,19], $h = 0.5$–$5.0$ mm is analyzed. In this analysis, first, the main model in Fig. 3 (a) consisting of larger elements is analyzed to obtain the displacements. Next, the sub-model in Fig. 3 (b) consisting of smaller elements is analyzed by using the obtained displacement. Then. the ISSF is calculated from the

**Table 2**
Mesh independency of FEM stress ratio (ρ/W=0.01, h/W=0.0236).

(a) At straight side

| $y/W$ | $\frac{\sigma_{z\,FEM}\mid_{h/W=0.01}}{\sigma_{z\,FEM}\mid_{h/W\geq 1}}$ | |
|---|---|---|
| | $e_{min} = 1/4000$ mm | $e_{min} = 1/8000$ mm |
| 0.000 | 0.291 | 0.289 |
| 0.100 | 0.291 | 0.290 |
| 0.200 | 0.292 | 0.290 |
| 0.300 | 0.292 | 0.291 |
| 0.400 | 0.294 | 0.292 |
| 0.450 | 0.290 | 0.288 |
| 0.490 | 0.244 | 0.243 |

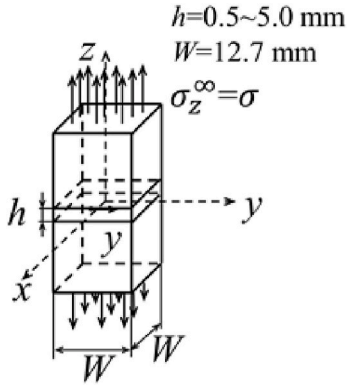


(b) At fillet

| $\theta$ | $\frac{\sigma_{z\,FEM}\mid_{h/W=0.01} - \widetilde{\sigma}_{z\,FEM}}{\sigma^{2D}_{z\,FEM}\mid_{h/W\geq 1}}$ | |
|---|---|---|
| | $e_{min} = 1/4000$ mm | $e_{min} = 1/8000$ mm |
| 0 | 0.244 | 0.243 |
| 9 | 0.252 | 0.251 |
| 18 | 0.258 | 0.257 |
| 27 | 0.262 | 0.261 |
| 36 | 0.265 | 0.264 |
| 45 | 0.266 | 0.265 |

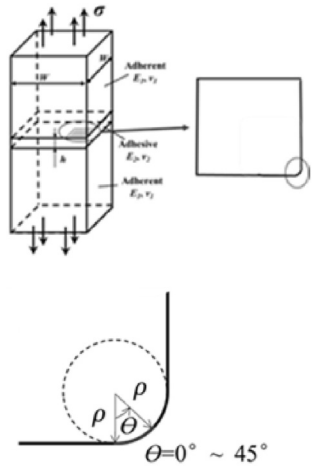

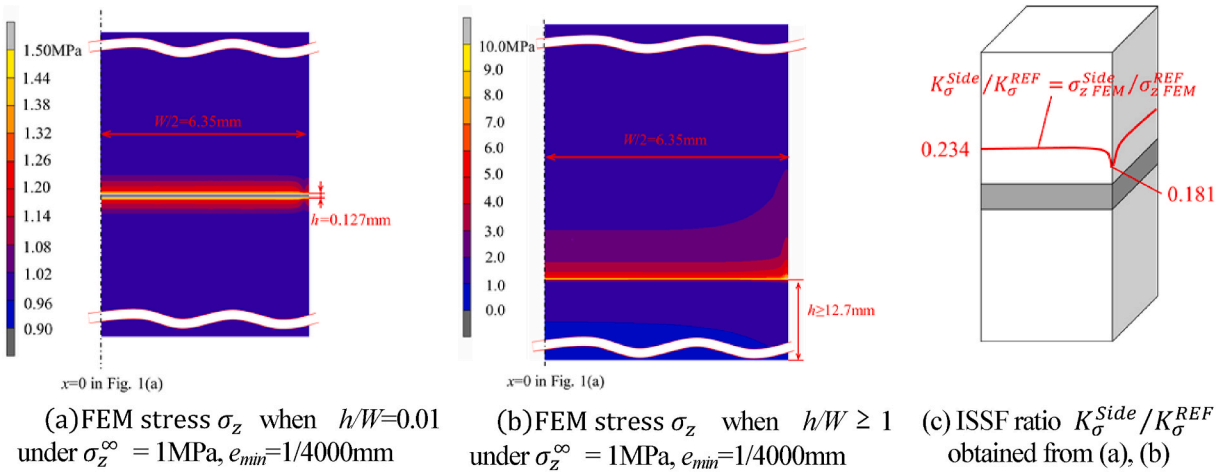


**Fig. 6.** Example of contour plots of FEM Stress $\sigma_z$ and ISSF ratio distribution when $\rho/W = 0.01$.

submodel confirming mesh-independency [10]. The analysis model is composed of 8-node hexahedral elements as shown in Fig. 3. The FEM software MSC Marc/Mentat 2012 is used as the analysis code in this study.

Fig. 5 illustrates the analysis model for the specimen used in the experiment when the corner fillet has the radius $\rho = a$. The ISSF $K_\sigma(y)$ can be defined from the real stress $\sigma_{z\,Real}(r,y)$ along the interface side in Fig. 1 and the ISSFs $K_\sigma(\theta)$ can be defined from the real stress $\sigma_{z\,Real}(r,\theta)$ around the corner fillet in Fig. 5 as shown in Eq. (3).

$$K_\sigma(y) = \lim_{r\to 0}\left[r^{1-\lambda} \times \sigma_{z\,Real}(r,y)\right]$$
$$K_\sigma(\theta) = \lim_{r\to a}\left[(a-r)^{1-\lambda} \times \sigma_{z\,Real}(r,\theta)\right] \tag{3}$$

The normalized ISSFs $F_\sigma(y)$, $F_\sigma(\theta)$ can be expressed by Eq. (4). Here, $\sigma_z^\infty$ denotes the remote tensile stress as shown in Fig. 1.

$$F_\sigma(y) = \frac{K_\sigma(y)}{\sigma_z^\infty W^{1-\lambda}} = \frac{\lim_{r\to 0}\left[r^{1-\lambda} \times \sigma_{z\,Real}(r,y)\right]}{\sigma_z^\infty W^{1-\lambda}}$$
$$F_\sigma(\theta) = \frac{K_\sigma(\theta)}{\sigma_z^\infty W^{1-\lambda}} = \frac{\lim_{r\to a}\left[(a-r)^{1-\lambda} \times \sigma_{z\,Real}(r,\theta)\right]}{\sigma_z^\infty W^{1-\lambda}} \tag{4}$$

In Eq. (4), $F_\sigma(\theta)$ is normalized by $\sigma_z^\infty W^{1-\lambda}$ to be compared with $F_\sigma(y)$ [10] at the straight edge. In Eqs. (3) and (4), $\lambda$ is a singularity index, which can be obtained from the eigen equation (5) [15,16].

$$\left[\sin^2\left(\frac{\pi}{2}\lambda\right) - \lambda^2\right]^2\beta^2 + 2\lambda^2\left[\sin^2\left(\frac{\pi}{2}\lambda\right) - \lambda^2\right]^2\alpha\beta + \lambda^2\left[\lambda^2 - 1\right]\alpha^2 + \frac{\sin^2(\lambda\pi)}{4} = 0 \tag{5}$$

$$\alpha = \frac{G_1(\kappa_2+1) - G_2(\kappa_1+1)}{G_1(\kappa_2+1) + G_2(\kappa_1+1)}\ ,\ \beta = \frac{G_1(\kappa_2-1) - G_2(\kappa_1-1)}{G_1(\kappa_2+1) + G_2(\kappa_1+1)} \tag{6}$$

$$\kappa_j = \begin{cases} \dfrac{3-\nu_j}{1+\nu_j} & (plane\ stress) \\ 3-4\nu_j & (plane\ strain) \end{cases} \quad (j=1,\ 2) \tag{7}$$

Here, $\alpha$, $\beta$ are Dundurs parameters [15,16] defined from Poisson's ratio $\nu_j$ and shear modulus $G_j$ of the adherend and adhesive ($j = 1$ for the adherend, $j = 2$ for the adhesive) as shown in Eqs. (6) and (7). It is known that when $\alpha$ ($\alpha$-2$\beta$) > 0 the real stress $\sigma_{z\,Real}$ has a singularity of the form $\sigma_{z\,Real} \propto 1/r^{1-\lambda}$ ($\lambda < 1$) [7–10]. Table 1 shows the mechanical properties of the adherend and the adhesive used in the experiment with Dundurs parameter $\alpha$, $\beta$ and singularity index $\lambda$ [15,16].

Since the FEM stress $\sigma_{z\,FEM}$ varies depending on the mesh size, the ISSF cannot be obtained from Eqs. (3) and (4). However, by applying the same mesh pattern to the unknown and the reference problems around the interface edge, the FEM stress ratio can be mesh-independent as shown in the previous study [7–10]. This is because the error of the FEM stress ratio can be canceled under the same mesh [7–10]. The exact ISSF of the unknown problem can be obtained by multiplying the FEM stress ratio and the exact ISSF of the reference solution. The following relationship can be confirmed from the reference problem ($K_\sigma^{REF}$, $F_\sigma^{REF}$, $\sigma_{z\,FEM}^{REF}(r)$) and the unknown problem ($K_\sigma$, $F_\sigma$, $\sigma_{z\,Real}(r)$). Here, $\lambda$ and $\sigma_z^\infty$ are the same for the reference problem and the unknown problem.

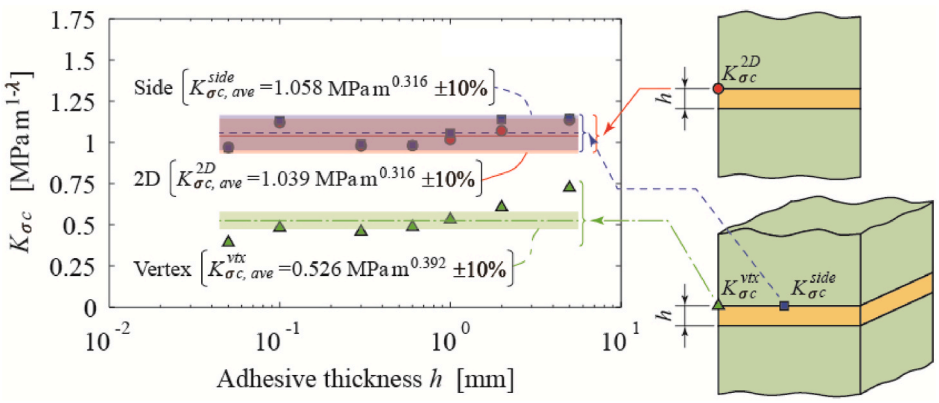


**Fig. 7.** Critical ISSF obtained from 2D and 3D analysis.

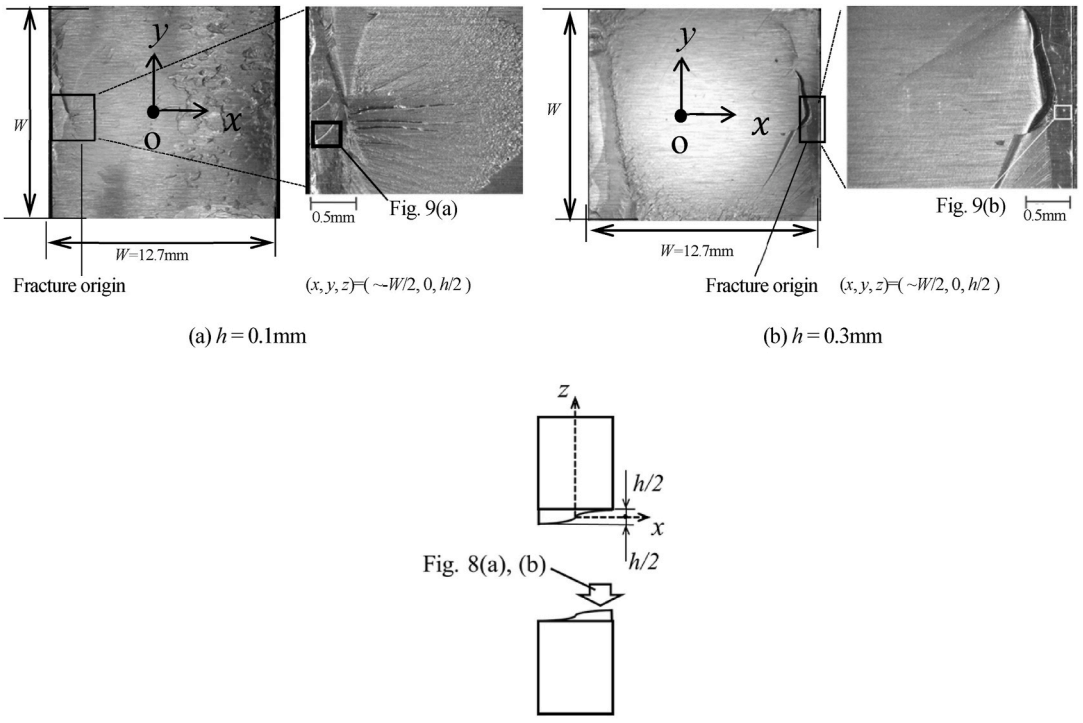


**Fig. 8.** Fractured surface of the butt joint specimens focusing on the fracture origin on the surface in Fig. 8(c).

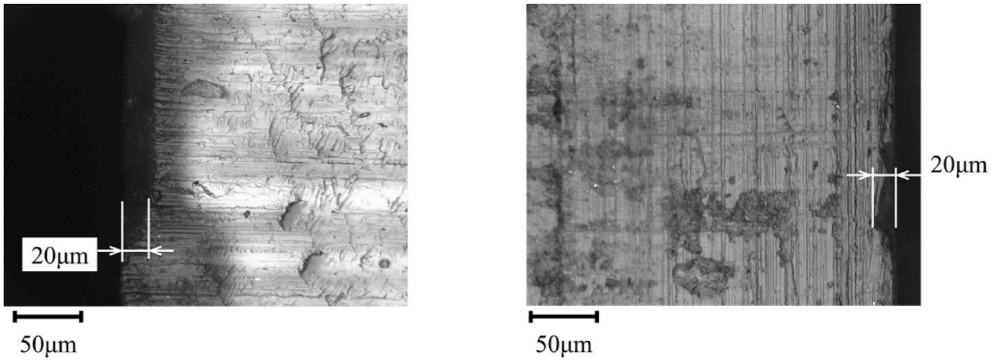


**Fig. 9.** Detail of fracture origin in Fig. 8(a) and (b) whose size is about 20 μm observed on the surface in Fig. 8(c).

$$\frac{K_\sigma}{K_\sigma^{REF}}=\frac{F_\sigma\sigma_z^\infty W^{1-\lambda}}{F_\sigma^{REF}\sigma_z^\infty W^{1-\lambda}}=\frac{\lim_{r\to0}\left[r^{1-\lambda}\times\sigma_{z\,Real}(r)\right]}{\lim_{r\to0}\left[r^{1-\lambda}\times\sigma_{z\,Real}^{REF}(r)\right]}=\lim_{r\to0}r^{1-\lambda}\times\sigma_{z\,Real}(r)=\frac{\sigma_{z\,FEM}(r)}{\sigma_{z\,FEM}^{REF}(r)}$$

but $\sigma_{z\,FEM}\neq\sigma_{z\,Real}$ (8)

### 2.3. Mesh independency showing that the FEM ratio can be regarded as the ISSF ratio

Table 2 shows an example of the FEM stress ratio based on small strain-small displacement analysis. Here, the two-dimensional bonded plate whose exact solution is available can be used as the reference problem. Table 2 (a) shows FEM stress ratio $\sigma_{z\,FEM}|_{h/W=0.01}/\sigma_{z\,FEM}^{2D}\,|_{h/W\geq1}$ along the interface side. Table 2 (b) shows the FEM stress ratio $(\sigma_{z\,FEM}|_{h/W=0.01}-\widetilde{\sigma}_{z\,FEM})/\sigma_{z\,FEM}^{2D}\,|_{h/W\geq1}$ around the corner fillet. The previous study [9] showed that the non-singular term $\widetilde{\sigma}_{z\,FEM}$ appears at the corner fillet, which is expressed by Eq. (9).

$$\widetilde{\sigma}_{z\,FEM}=-\frac{(\nu_1-\nu_2)E_1E_2}{(1+\nu_1)\nu_1E_2-(1+\nu_2)\nu_2E_1}\varepsilon_\theta \tag{9}$$

Here, $\varepsilon_\theta$ is the strain in the $\theta$-direction in Fig. 4. As shown in Table 2, the ratio of FEM stress is mesh-independent at the straight interface side and the corner fillet. As shown in Table 2, the ISSF can be obtained accurately from the ISSF ratio.

### 2.4. Effect of the bondline thickness h on the ISSF

Fig. 6 shows examples of the contour plot of FEM stress when $\rho/W=0.01$. Fig. 6 shows FEM stress $\sigma_z$ when (a) $h/W=0.01$, Fig. 6 (b) shows FEM stress $\sigma_z$ when (b) $h/W\geq1$. Note that in Fig. 6 (c) shows the FEM stress ratio but it can be regarded as the exact ISSF ratio. Those figures are useful for understanding the effect of $h$ on the ISSF. As shown in Fig. 6 (a), when $h$ is smaller, FEM stress is comparatively smaller especially at the interface corner due to the interaction of ISSFs at $z=\pm h/2$.

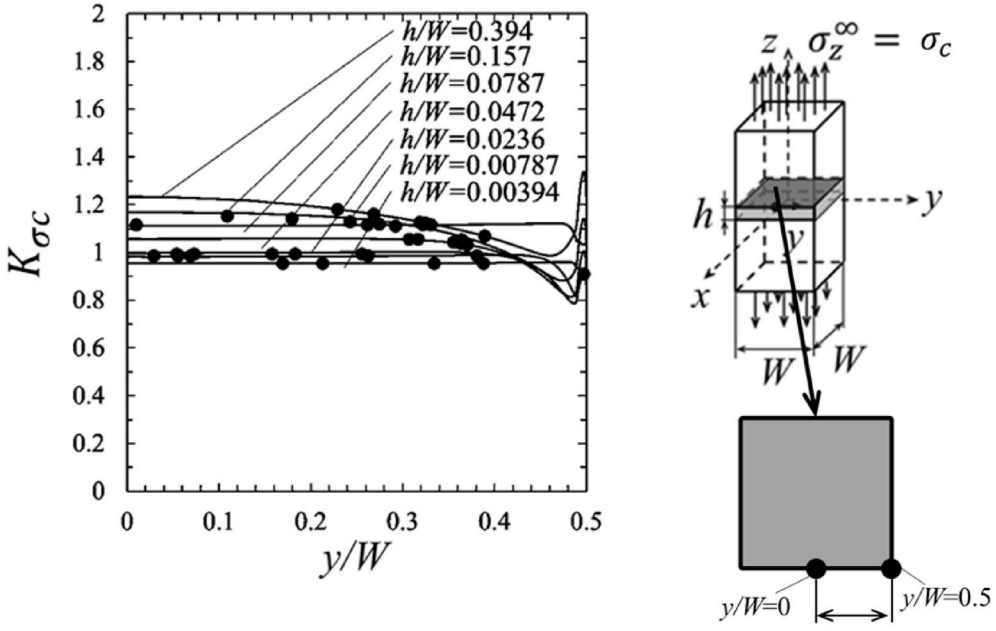


(a) ISSF for $0 \leq y/W \leq 0.5$

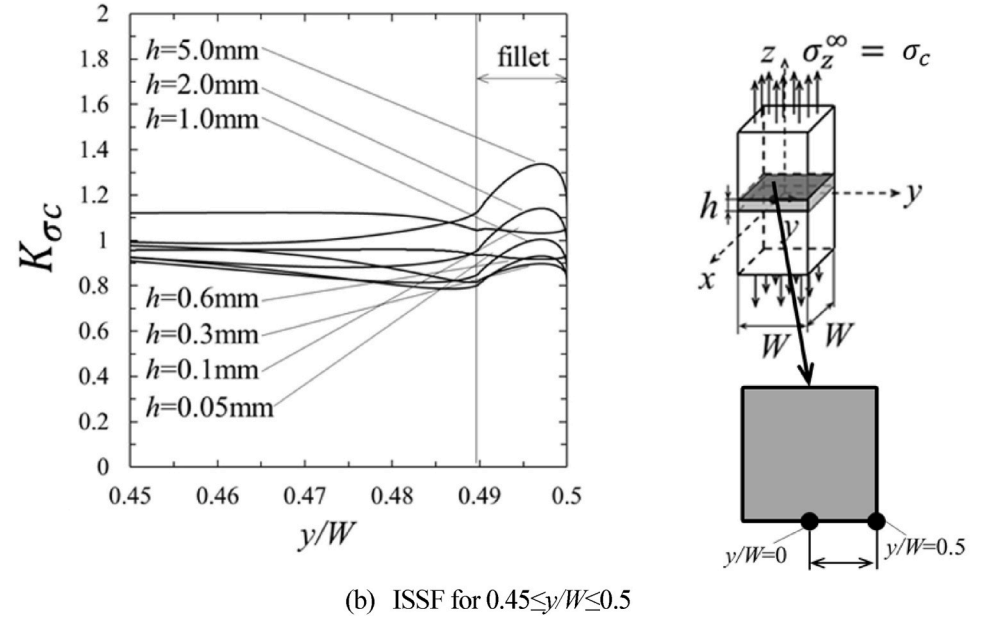


(b) ISSF for $0.45 \leq y/W \leq 0.5$

**Fig. 10.** Critical ISSF distributions by varying adhesive thickness.

Instead, as shown in Fig. 6 (b), when $h/W \geq 1$, FEM stress is relatively larger especially at the corner. With decreasing $h$, the ISSS decreases due to the interaction of the two interfaces $z = \pm h/2$ as shown in Fig. 2(b). This is the reason why the debonding strength in Fig. 1 can be expressed as a constant ISSF as shown in Fig. 2(c).

### 2.5. Validity of 2D ISSF analysis

Compared to the 3D analysis discussed above, the simple 2D analysis can be used conveniently. Fig. 7 shows the critical ISSFs at the center of the interface $K_{\sigma c}(0)$ obtained from the 3D analysis in comparison with the ISSF obtained from the plane strain 2D analysis. In Fig. 7, the 3D constant value of $K_{\sigma c}(0) = 1.058 \pm 0.080$[MPa·m$^{0.315}$] is almost the same as the 2D constant value $K_{\sigma c}^{2D} = 1.039 \pm 0.0643$[MPa· m$^{0.315}$] in Fig. 2(c). Moreover, in Fig. 7, the critical ISSF $K_{\sigma c}^{vtx}$ at the corner is also indicated where the debonding occurs. The critical ISSF $K_{\sigma c}^{vtx}$ obtained from the 3D analysis. As shown in Fig. 7, the adhesive strength can be expressed as $K_{\sigma c}^{2D} = \text{const.}, K_{\sigma c}(0) = \text{const.}$ or $K_{\sigma c}^{vtx} = \text{const.}$ independent of $h$. By using one of the three, the adhesive strength can be expressed; and therefore, the validity of the 2D analysis is confirmed.

## 3. Fracture origin identification when the adhesive strength can be expressed as a constant ISSF

### 3.1. Fracture origin of butt joints

Fig. 8 shows an example of the butt joint's whole fractured surface of $h = 0.1$ mm and $h = 0.3$ mm [10]. The large amount of adhesive remains on those fractured surfaces in Fig. 8(a) and (b) as illustrated in Fig. 8(c). Bonded surface are ground mechanically by using WAH-60 (white aluminum oxide, No. 60, grain size) grinding wheel. The figure on the left is the whole fractured surfaces, and the figure on the right is an

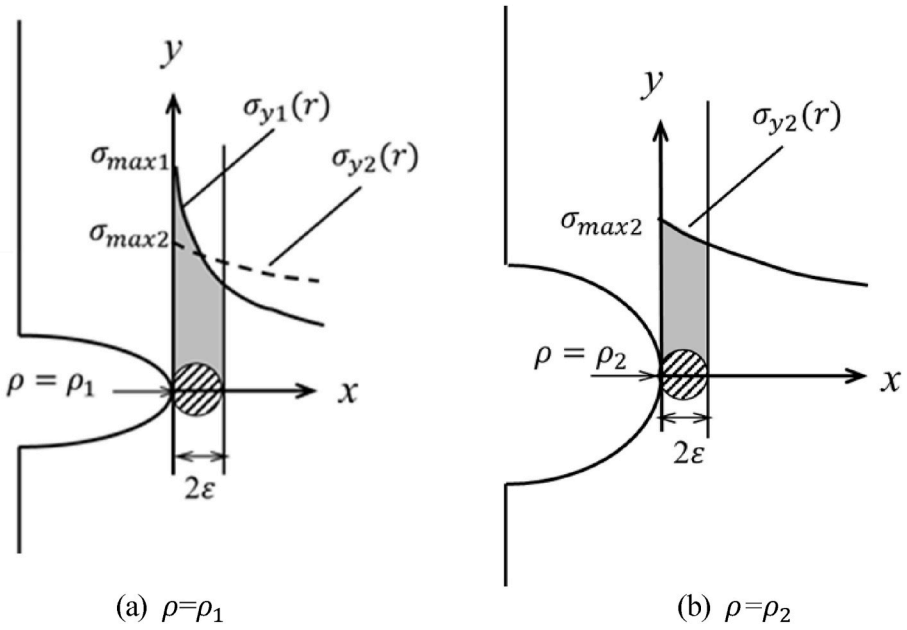


**Fig. 11.** An example of difference stress distributions but the same damage appears for 2D notch.

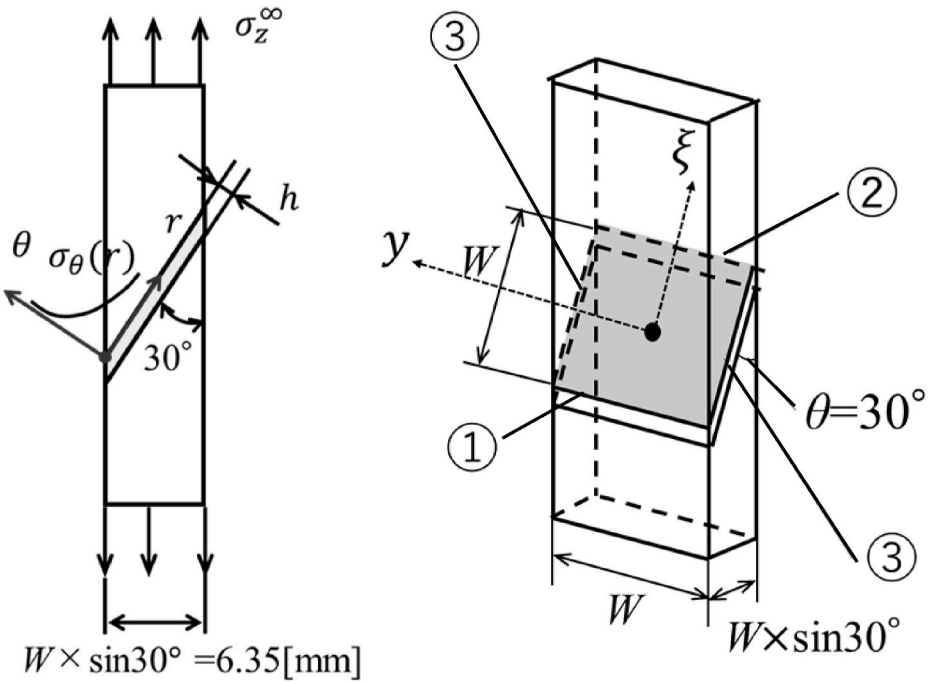


**Fig. 12.** Prismatic scarf joint.

enlarged view ( × 50) around the fracture origin. As shown in Fig. 8, for almost all specimen the fracture originates from the interface side away from the corners. The detail is indicated in Section 3.2 in relation to the ISSF variation. Fig. 9 shows the detail of fracture origin in Fig. 8(a) and (b). As shown in Fig. 9, the fracture originates from a dent whose depth is about 20 μm at the adhesive surface at $|x| = W/2$ in Fig. 1. Those dents are formed due to the machining the $xy$ plane at $|z| = h/2$ of the bonded surface before bonding in the $y$-direction in Fig. 1. Since the $yz$ surface of Fig. 1 at $|x| = W/2$ is polished in the z-direction by using sandpaper from # 400 to # 1000 in order to remove the adhesive protruding to the edge of the adhesive layer, dents may be formed affected by those machining and polishing at the intersection $|x| = W/2$ and $|z| = h/2$. It may be conjectured that those dents can be origins of the fracture.

### 3.2. Position of the fracture origin in relation to the ISSF in prismatic butt joints

In this section, the position where the fracture origin is described in terms of the ISSF discussed in Section 2.2. The detail can be found in the previous papers [10,18,19]. Fig. 10 shows the ISSF variations when debonding stress $\sigma_z^\infty = \sigma_c$ is applied. Here, the fracture origins are denoted by the solid circles for different bondline thickness $h$. From Fig. 10, it is seen that the maximum ISSF at the side is almost equal to the maximum ISSF at the corner when $h \leq 2.0$ mm ($h/W \leq 0.157$). However,

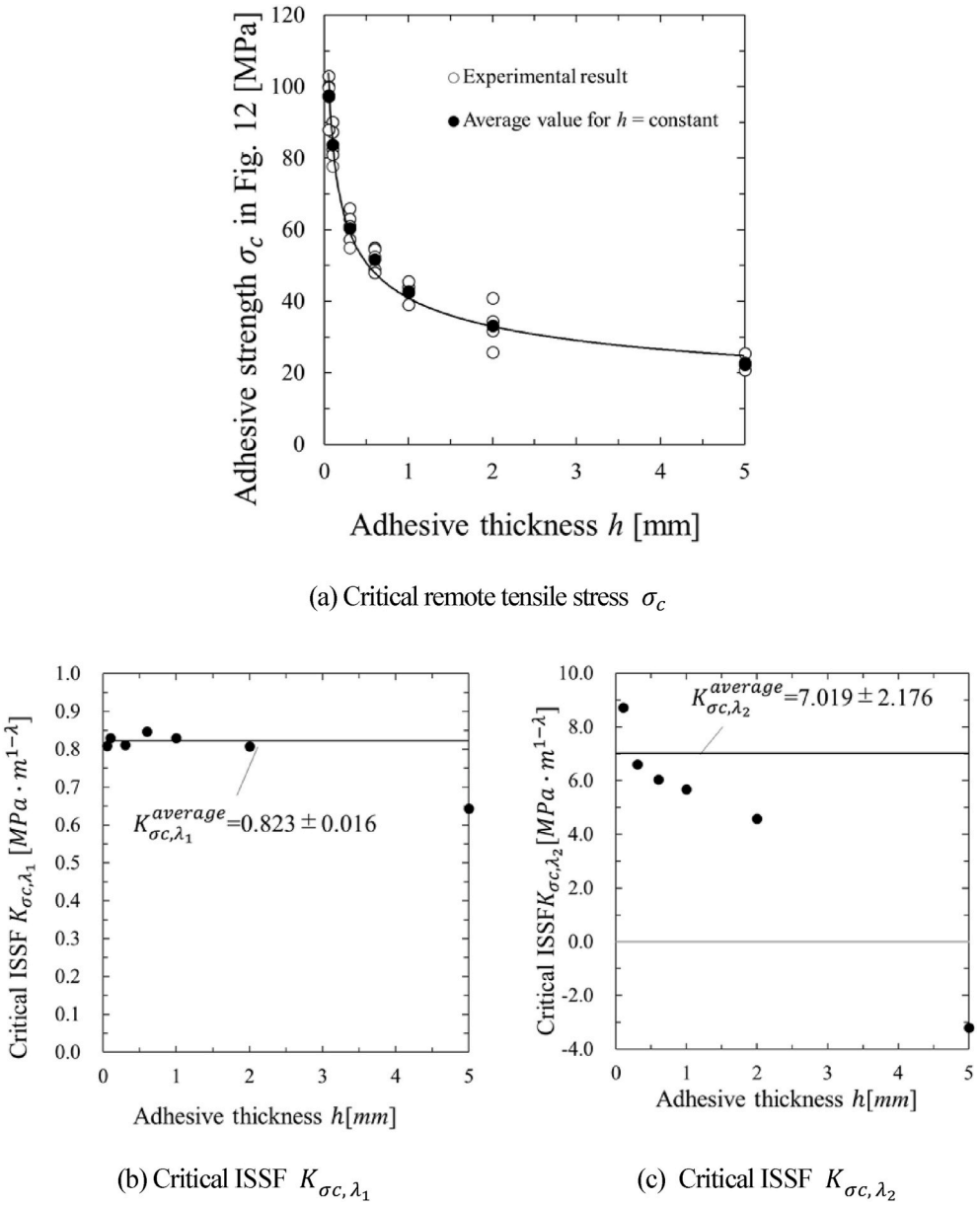


**Fig. 13.** Debonding strength for scarf joint.

most of the fractures originate from the interface side instead of the interface corner because the maximum ISSF exists in a certain range at the middle of the interface side. Instead, the maximum ISSF always exists in a limited region at the interface corner and the fracture hardly occurs at the corner. The peak ISSF appears reflecting the corner point singularity at $y/W = 0.5$ when $\rho \to 0$. At the corner, only one fracture origin is found when $h = 0.05$ mm ($h/W = 0.00394$) as shown in Fig. 10 (a). This is because the ISSF variation is almost constant as shown in Fig. 10 (b) when $h = 0.05$ mm. Instead, when $h = 5$ mm, for example, although the ISSF at the fillet is larger than the ISSF at the center of the side, the fracture originates from the side since the ISSF at the fillet is extremely localized in the circumferential direction.

One may think that why the fracture does not occur at the maximum position of the ISSF. Since it is known that the brittle and fatigue fracture is controlled by the larger stress region size (large ISSF region size) as well as the maximum stress (the maximum ISSF), an example is explained by using a simple 2D notch. Fig. 11 (a), (b) shows an example where the same damage appears under different maximum stress at the notch root. Since the fracture process zone size is about $2\varepsilon$, two notches $\rho = \rho_1$ and $\rho = \rho_2$ are equivalent since the $2\varepsilon$ process zone is subjected to almost the same severity [20]. If the fracture process zone size becomes larger, for example, $4\varepsilon$, the stress of the notch $\rho = \rho_2$ becomes more severe and more like to be fractured even though the maximum stress is smaller than the maximum stress for $\rho = \rho_1$. Similarly, when $h = 5$ mm in Fig. 10, although the ISSF at the fillet is larger than the ISSF at the center of the side, the ISSF at the fillet is extremely localized in the circumferential direction. In this way, the certain constant of large ISSF region is necessary for the fracture origin. Therefore, the fracture does not occur at the corner although the maximum ISSF value is situated at the corner.

### 3.3. Fracture origin of scarf joints when the adhesive strength can be expressed as a constant ISSF

Fig. 12 shows the prismatic scarf joint specimen. Regarding the scarf joint with the scarf $\theta = 30°$ in Fig. 12, different from the butt joint ($\theta = 90°$), two distinct singular stress fields appear along the interface. They correspond to two distinct singularity indices. The interface stress $\sigma_\theta(r)$

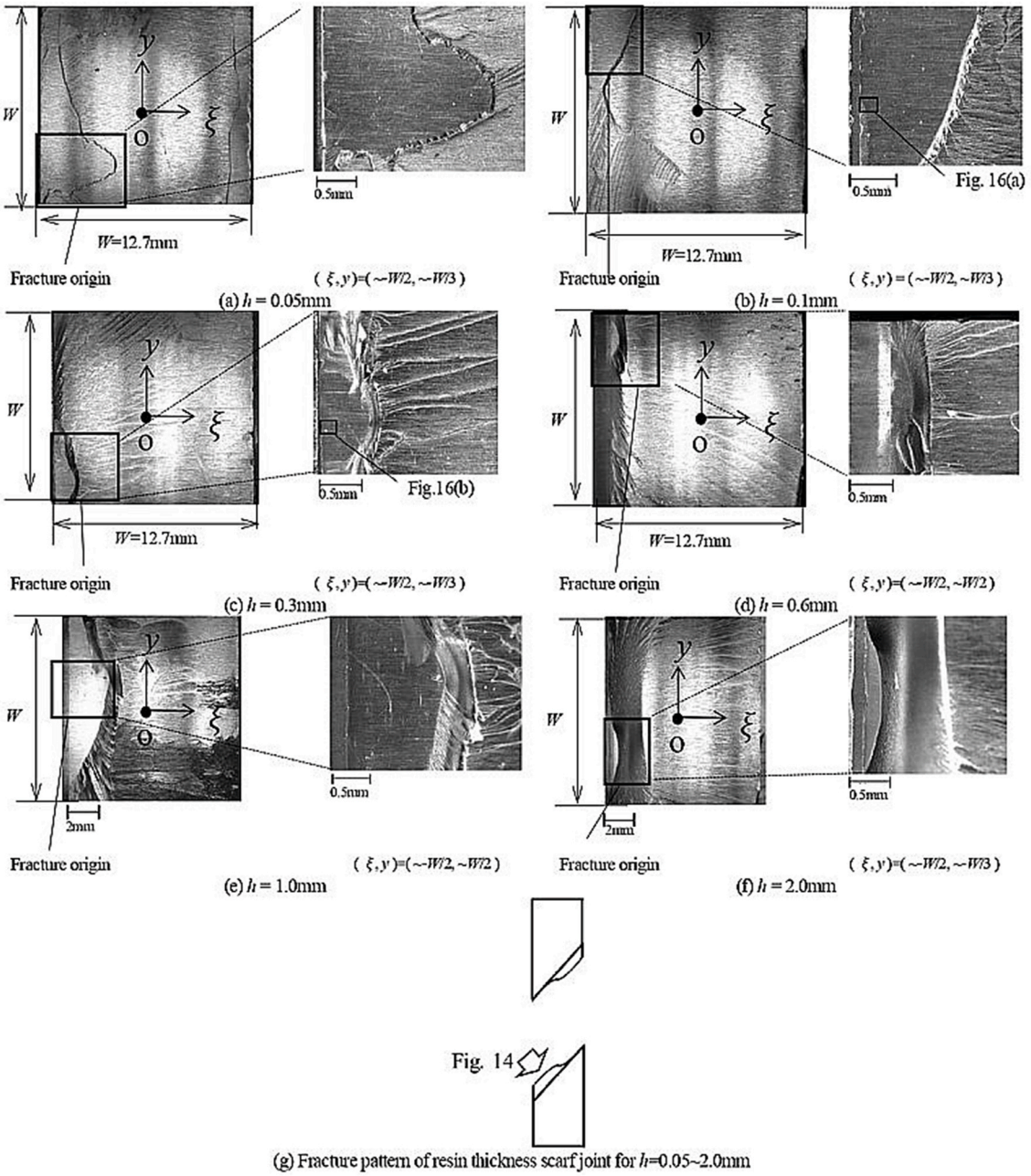


**Fig. 14.** Fractured surface of the scarf joint focusing on the fracture origin when $0.05 < h < 2.0$ on the surface in Fig. 14 (g).

at a distance $r$ from the interface end can be expressed by Eq. (10).

$$\sigma_\theta(r) = \frac{K_{\sigma,\lambda_1}}{r^{1-\lambda_1}} + \frac{K_{\sigma,\lambda_2}}{r^{1-\lambda_2}} \tag{10}$$

For Resin A/Steel, the singular indices are $\lambda_1 = 0.737$ and $\lambda_2 = 0.977 \cong 1$. From $\lambda_2 - \lambda_1 = 0.240 > 0$ and $K_{\sigma,\lambda_2}/K_{\sigma,\lambda_1} \cdot r^{\lambda_2-\lambda_1} \ll 1$ near the interface end as $r \to 0$. In other words, the first term of the two singular stresses becomes dominant as can be expressed $\sigma_{\theta,\lambda_1} \to K_{\sigma,\lambda_1}/r^{1-\lambda_1}$ when $r \to 0$.

$$\sigma_\theta(r) = \frac{K_{\sigma,\lambda_1}}{r^{1-\lambda_1}}\left(1 + \frac{K_{\sigma,\lambda_2}}{K_{\sigma,\lambda_1}} r^{\lambda_2-\lambda_1}\right) \to \frac{K_{\sigma,\lambda_1}}{r^{1-\lambda_1}} \quad (r \to 0) \tag{11}$$

In this study, two distinct ISSFs are obtained accurately on the basis of the previous study [21]. Fig 13 (a) shows the critical remote tensile stress $\sigma_c$ where the solid black circle denotes the average value obtained from 5 experiment results under $h = \text{const.}$ Fig. 13 (b) shows the critical ISSF $K_{\sigma c,\lambda_1}$ and Fig. 13(c) shows the critical ISSF $K_{\sigma c,\lambda_2}$. As shown in Fig. 13(b), by using the first term of the ISSF $K_{\sigma c,\lambda_1} = \text{const.}$ the average adhesive strength can be expressed as a constant value within 2% error. Fig. 13(c) shows the second term of the critical ISSF $K_{\sigma c,\lambda_2}$ is not constant because the second singular stress field is relatively small as $r \to 0$ as shown in Eq. (11). This critical ISSF $K_{\sigma c,\lambda_1} = 0.823 \pm 0.016$ MPa·m$^{0.263}$ in Fig. 13(b) is much smaller than the critical ISSF of butt joint $K_{\sigma c} = 1.039 \pm 0.0643$ MPa·m$^{0.315}$ in Fig. 2(c). In this paper, the singular stress $\sigma_\theta(r)$ at interface end is focused for scarf and butt joints. The interface shear stress $\tau_{r\theta}$ of scarf joint is much larger than the one of butt joint. This is the reason why the critical ISSF of scarf joint $K_{\sigma c,\lambda_1}$ is much smaller than the critical ISSF of butt joint $K_{\sigma c}$. The reason why the critical ISSF of $h = 5.0$ mm is smaller than the one of $h = 0.05$–$2.0$ mm will be described later. Previously, Mintzas et al. [6] reported that the Suzuki's experimental results can be expressed as a constant value of the ISSF. However, in their analysis [6], only the first term singular stress field was considered and relatively small critical value of the ISSF for $h = 5.0$ mm

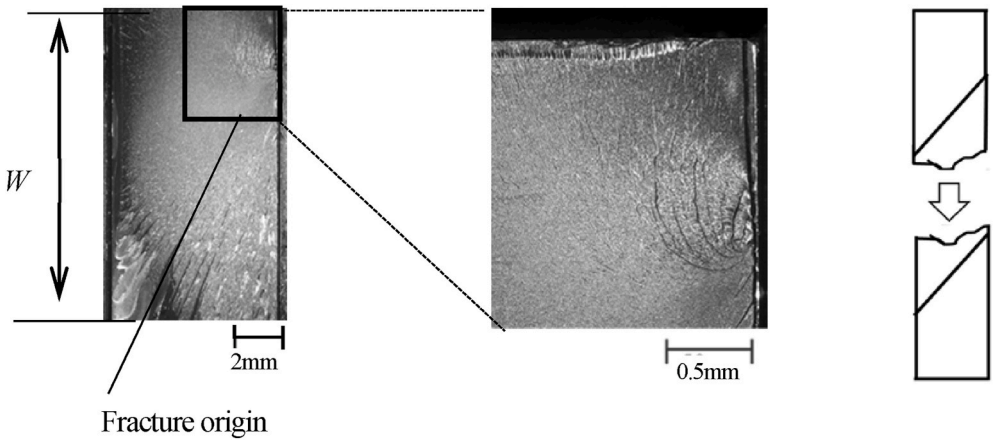


**Fig. 15.** The fractured surface in the scarf joint focusing on the fracture origin when $h = 5.0$ mm.

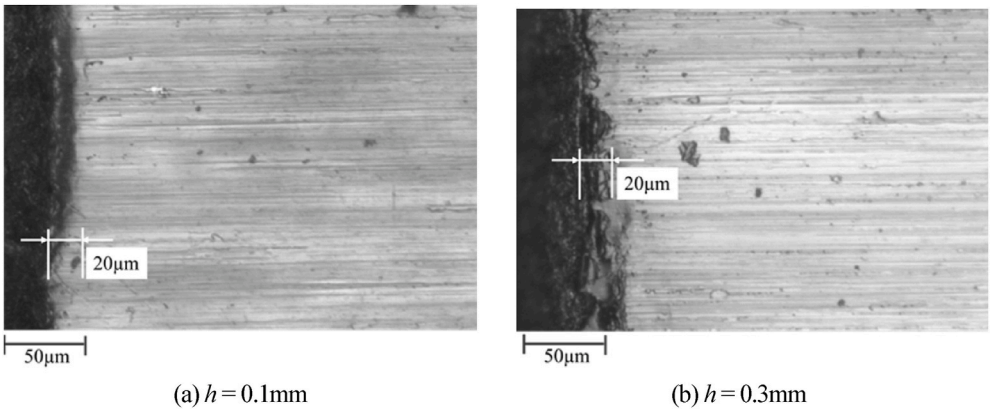


**Fig. 16.** Detail of fracture origin in Fig. 14(b) and (c).
whose size is about 20 μm observed on the surface in Fig. 14 (g) when $h \leqq 2.0$ mm.

was not indicated. Chen-Nisitani [22] clarified that when two singular stress fields are approximated by one singular stress field, the expression varies depending on the distance $r$ and hardly expressing two distinct singular stress fields.

Figs. 14 and 15 show an example of the scarf joint's whole fractured surface when the adhesive layer thickness $h = 0.05$–$5.0$ mm. The large amount of adhesive remains on those fractured surfaces in Fig. 14(a)–(f) as illustrated in Fig. 14(g). The figure on the left is the whole fractured surfaces whose shape is a square as shown in Fig. 12 [18,19], and the figure on the right is an enlarged view of the area around the fracture origin. The observation shows that all of the fractures occur from the side of $\xi = -W/2$ (Fig. 12 ①) to the $y = \pm W/2$ (Fig. 12 ③) then extend to $\xi = +W/2$ (Fig. 12 ②) when $h = 0.05$–$2.0$ mm.

It should be noted that when the adhesive bondline thickness $h = 5.0$ mm there is no fracture near the adhesive interface. As shown in Fig. 15, when $h = 5.0$ mm the fracture occurs across the adhesive layer. This is the reason why the average adhesive strength of $h = 5.0$ mm is 20% lower than the other average adhesive strength, which can be expressed as a constant ISSF as $K_{\sigma c,\,\lambda_1} = 0.823 \pm 0.016$ MPa·m$^{0.263}$ for $h = 0.05$–$2.0$ mm in Fig. 13(b). Instead, regarding the butt joint, the average adhesive strength can be always expressed as $K_{\sigma c} = 1.039 \pm 0.0643$ MPa·m$^{0.315}$ for $h = 0.05$–$5.0$ mm within 7% error as shown in Fig. 2(c). This is because as shown in Fig. 8 (c) the butt joint fracture pattern of resin thickness occurs always near the interface as shown in Fig. 8 (c). Therefore, it may be concluded that when the cohesive fracture near the bonded surface occurs the sufficient adhesive strength is obtained and the strength can be expressed as a constant value of the ISSF. Fig. 16 shows examples of fracture origin with the magnification 1000 when $h = 0.1$ mm and $h = 0.3$ mm. As shown in Fig. 16, for scarf joints with h = 0.05–2.0 mm, the fracture originates from a dent whose depth is about 20 μm at the interface side.

## 4. Cohesive fracture verification when the adhesive strength can be expressed as a constant ISSF

### 4.1. Cohesive fracture confirmation on whole fractured surface for resin A

In this Section, the fractured surface is examined to confirm the fracture is cohesive or not. In the previous Section 3, the fractured surfaces where the large amount of adhesive remains near the fracture origin were discussed to identify the fracture origin. This is because in Figs. 8 and 14, since the large amount of adhesive remains, the fracture origin can be identified more easily. In this Section, however, the other surface side where the slight amount of adhesive remains is focused. This is because to confirm the cohesive fracture the slight amount of adhesive should be identified on this side. Fig. 17(c) shows an example of the butt joint's whole fractured surface where the slight amount of adhesive remains near the fracture origin when $h = 0.1$ mm. As shown in Fig. 17(c), typical adhesive fracture pattern named "Mirror, Mist, and Hackle" [18,19] can be seen even though the adhesive amount is not very large near the fracture origin.

Fig. 17(d) shows an example of the scarf joint's whole fractured surface where the slight amount of adhesive remains when $h = 0.3$ mm. As shown in Fig. 17(d), another typical adhesive pattern named "Feather-like pattern" [18,19] can be seen even though the adhesive

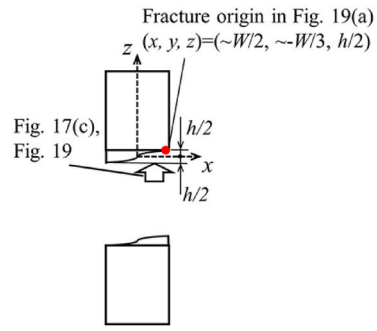


(a) Fracture pattern of resin thickness for butt joint for $h$=0.05~5.0mm

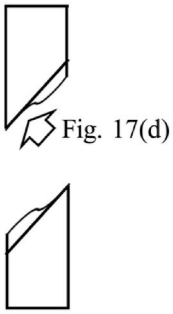


(b) Fracture pattern of resin thickness for scarf joint for $h$=0.05~2.0mm

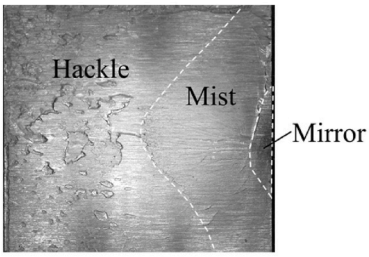


(c) Typical cohesive fracture surface named "Mirror, Mist and Hackle" ($h$=0.1mm)

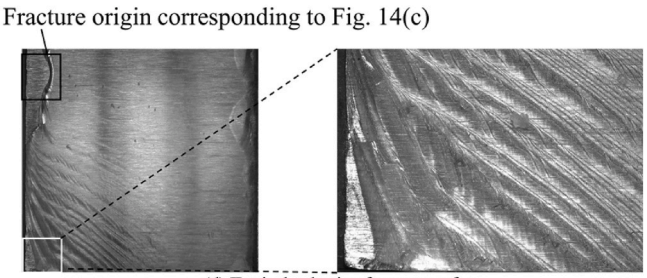


(d) Typical cohesive fracture surface named "Feather-like pattern" ($h$=0.3mm)

**Fig. 17.** Cohesive fracture confirmation for the surface in Fig. 17(a), (b) where the slight amount of adhesive remains near the fracture origin.

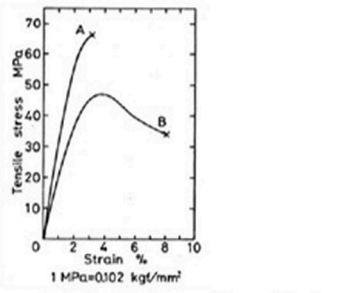


(a) Stress-Strain curve for bulk adhesive specimen of Resin A, B [18, 19]

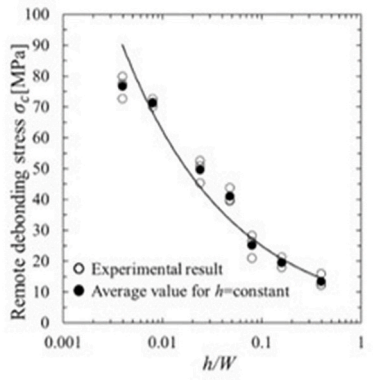


(b) Critical remote tensile stress $\sigma_c$ for Steel/ /Resin B

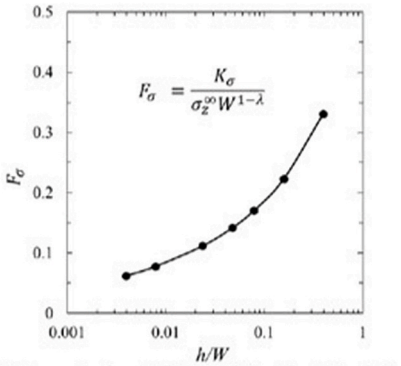


(c) Dimensionless ISSF $F_\sigma^{Side}$ for Steel/ /Resin B obtained by 2D modelling

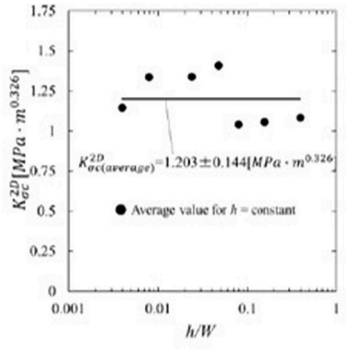


(d) Critical ISSF for Steel/ /Resin B

**Fig. 18.** Bulk adhesive strength for resin A, B and debonding strength for Steel/Epoxy Resin B.

**Table 3**
Material properties for Steel/Epoxy Resin B [18,19].

| Material | | Young's modulus$E$ [GPa] | Poisson's ratio$\nu$ | Bulk strength $\sigma_B$ [MPa] | $\alpha$ | $\beta$ | Butt joint | Scarf joint | |
|---|---|---|---|---|---|---|---|---|---|
| | | | | | | | $\lambda$ | $\lambda_1$ | $\lambda_2$ |
| Adherend | S35C | 206 | 0.30 | 570 | 0.978 | 0.188 | 0.674 | 0.768 | 0.806 |
| Adhesive | Epoxy resin B | 2.16 | 0.38 | 46.8 | | | | | |

**Table 4**
Compositions of adhesives [14,18].

| Resin | Composition parts (weight ratio) | | |
|---|---|---|---|
| | Epikote 828 | Epikote 871 | DETA |
| A | 100 | 0 | 11.0 |
| B | 75 | 25 | 9.5 |

amount is not very large near the fracture origin. From those, typical adhesive fracture patterns as shown in Fig. 17 (c), (d), the cohesive fracture can be confirmed when the adhesive strength can be evaluated by constant ISSF. Therefore, it may be concluded that the ISSF evaluation method can apply when the fracture is cohesive as well as an interface fracture.

### 4.2. Cohesive fracture confirmation for resin B where the butt joint strength is larger than the bulk adhesive strength

Fig. 18 (a) shows the stress strain curve of bulk adhesive Resin A showing that the tensile strength $\sigma_B = 65.5$ MPa [14]. From Fig. 2 (a), when $h = 0.1$ mm ($h/W = 0.00787$), the adhesive butt joint strength for Steel/Resin A can be $\sigma_c = 58.8$ MPa, which is very close to the bulk adhesive strength. Fig. 18 (a) also shows the stress strain curve of bulk adhesive Resin B showing that the tensile strength $\sigma_B = 46.8$ MPa [14]. Table 4 shows the compositions of Resin A and Resin B [14,18]. Resin A is the epoxy resin of bisphenol A type Epikote 828 (Yuka Shell Epoxy Co.) by using diethylenetriamine (DETA) as hardener. Resin B consists of Epikote 828 and Epikote 871 by using DETA as hardener. Here, Epikote 871 is the flexible epoxy resin of dimer acid type (Yuka Shell Epoxy Co.). Resin A and Resin B are prepared corresponding to the mixture ratio as shown in Table 4. Fig. 18 (b) shows the adhesive butt joint strength $\sigma_c$ for Steel/Resin B [8–10]. As shown in Fig. 18 (b), when $h = 0.1$ mm ($h/W = 0.00787$) the adhesive strength of Steel/Resin B can be $\sigma_c = 71.4$ MPa, which is about 1.5 times larger than the bulk adhesive strength $\sigma_B = 48.6$ MPa of Resin B [14]. Such large strength cannot be obtained if those fractures are interface fractures although the typical adhesive fracture pattern such as mirror, mist, hackle and feather-like pattern cannot be seen for resin B [18,19]. In this way, 100% cohesive fracture can be confirmed for Resin A and Resin B. Fig. 18 (c) shows the normalized ISSF and Fig. 18(d) shows the critical ISSF can be expressed as $K_{\sigma c} = 1.203 \pm 0.144$ MPa m$^{0.326}$ of butt joint Steel/Resin B. As shown in Fig. 18 (a), Resin A is a brittle adhesive and Resin B is a ductile adhesive. Table 3 shows the mechanical properties of adhesive Resin B [18,19].

### 4.3. Cohesive fracture confirmation at fracture origin

Fig. 19(a) shows an example of the butt joint's whole fractured surface where the slight amount of adhesive remains near the fracture origin when $h = 1.0$ mm. In Fig. 19(a), the detail of the fracture origin is shown with the magnification 3000. For the reference, Fig. 19(b) shows the adherend steel surface with the magnification 3000 before applying the adhesive under the same processing conditions as the specimen used in the experiment. Differently from Fig. 19(b) and (a) shows a lot of patterns of minute irregularities throughout the photograph proving that the slight amount of adhesive remains due to the polished streaks of the adherend steel. Similar observation was reported by using SEM in the previous papers [18,19]. It may be concluded that even though the fracture originates from the interface end and the debonded surface looks like metal surface macroscopically the cohesive fracture can be confirmed. Therefore, it may be concluded that the ISSF evaluation

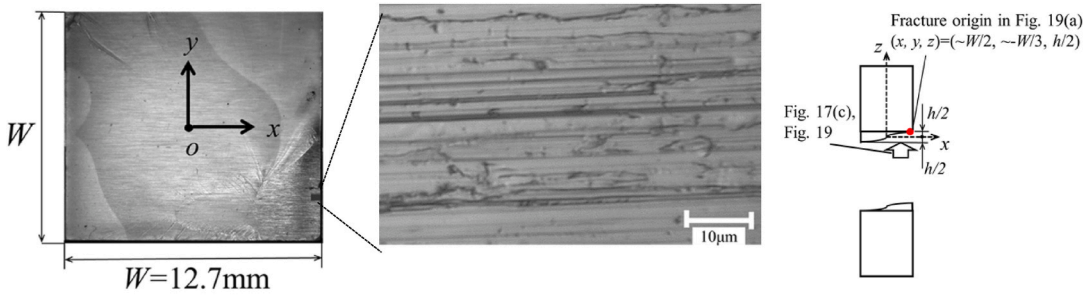


(a) Debonded surface where the slight amount of adhesive remains when $h = 1.0$mm at $(x, y, z) = (\sim W/2, \sim W/3, h/2)$ in Fig. 1

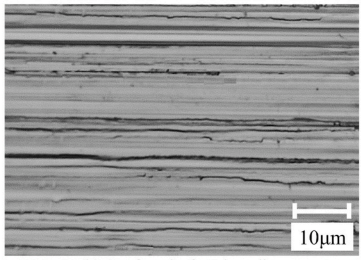


(b) Surface before bonding

**Fig. 19.** Cohesive fracture confirmation for the surface in Fig. 17(a)
where the slight amount of adhesive remains at the fracture origin when $h = 1.0$ mm.

method can apply when the fracture is cohesive as well as an interface fracture.

## 5. Conclusions

The aim of this paper is to explain that the ISSF evaluation method can apply when the fracture is cohesive as well as an interface fracture. Previously it was shown that the adhesive strength can be expressed as a constant value of the ISSF at the interface end for butt joints and lap joints. However, since the ISSF evaluation method is based on the singular stress field along the interface, many people may misunderstand that the method does not apply when the fracture is cohesive rather than an interface fractrue. Therefore, this study verified that the ISSF evaluation method can apply or not to cohesive fracture which is desirable for such adhesive joints. This study mainly focuses on the scarf joint which can be regarded as a general joint since it can be characterized between the butt and lap joints. The conclusions can be summarized in the following way.

(1) It is found that the fracture origin of the butt joint and scarf joint is the dent whose depth is about 20 μm situated on the side of the bonding interface. This origin at the interface end verifies the validity of the ISSF evaluation method. Those dents may be formed due to machining the bonded surface before bonding and polishing the edge of the adhesive layer.
(2) When the adhesive bondline thickness $h \geq 5.0$ mm, the fracture occurs across the adhesive layer and no fracture near the interface. This is the reason why the adhesive strength of $h = 5.0$ mm is lower than the strength of other $h = 0.05$–$2.0$ mm and the adhesive strength of $h = 5.0$ mm cannot be expressed as ISSF = constant differently from the other strength when $h = 0.05$–$2.0$ mm.
(3) The ISSF evaluation method can apply when the fracture is cohesive as well as an interface fracture. This is because even when the strength is expressed as a constant ISSF, the cohesive fracture was confirmed since the slight amount of adhesive remains on the fractured surface.
(4) Due to the roughness induced on the bonded surfaces appropriately, the cohesive usually occurs near the interface. This is the reason why the ISSF method can apply to the cohesive fracture. Since the fracture happens almost at the interface although the slight amount of adhesive remains, the fracture is controlled by the ISSF.

## References

[1] Barnes TA, Pashby IR. Joining techniques for aluminum spaceframes used in automobiles: part II – adhesive bonding and mechanical fasteners. J Mater Process Technol 2000;99:72–9.
[2] Petrie EM. Adhesives for the assembly of aircraft structures and components: decades of performance improvement, with the new applications of the horizon. Met Finish 2008;106(2):26–31.
[3] Jarry E, Shenoi RA. Performance of butt strap joints for marine applications. Int J Adhesion Adhes 2006;26(3):162–76.
[4] Encinas N, Oakley BR, Belcher MA, Blohowiak KY, Dillingham RG, Abenojar J, Martínez MA. Surface modification of aircraft used composites for adhesive bonding. Int J Adhesion Adhes ;50:157–63.
[5] Akisanya AR, Meng CS. Initiation of fracture at the interface corner of bi-material joints. J Mech Phys Solid 2003;51:27–46.
[6] Mintzas A, Nowell D. Validation of an Hcr -based fracture initiation criterion for adhesively bonded joints. Eng Fract Mech 2012;80:13–27.
[7] Zhang Y, Noda NA, Wu P, Duan ML. A mesh-independent technique to evaluate stress singularities in adhesive joints. Int J Adhes Adhes 2015; 57: 105–17; Corrigendum of authorship "A mesh-independent technique to evaluate stress singularities in adhesive joints". Int J Adhesion Adhes 2015;60:130.
[8] Noda NA, Miyazaki T, Li R, Uchikoba T, Sano Y, Takase Y. Debonding strength evaluation in terms of the intensity of singular stress at the corner with and without fictitious crack. Int J Adhesion Adhes 2015;61:46–64.
[9] Miyazaki T, Noda NA, Ren F, Wang Z, Sano Y, Iida K. Analysis of intensity of singular stress field for bonded cylinder and bonded pipe in comparison with bonded pipe. Int J Adhesion Adhes 2017;77:118–37.
[10] Takaki R, Noda NA, Sano Y, Takase Y, Suzuki Y, Chao CK. Fractographic identification of fracture origin mainly controlled by the intensity of singular stress field (ISSF) in prismatic butt joint with corner fillet. Int J Adhesion Adhes 2021; 106:102810.
[11] Matsumoto H. Understanding adhesive technology. Nihon Jitsugyo Publishing Co., Ltd.; 2018 [in Japanese].
[12] Brockmann W, Hennemann OD, Kollek H, Matz C. Adhesion in bonded aluminum joints for aircraft construction. Int J Adhesion Adhes 1986;6(3):115–43.
[13] Bikerman JJ. Causes of poor adhesion: weak boundary layers. Ind Eng Chem 1967; 59(9):40–4.
[14] Suzuki Y. Adhesive engineering. Maruzen Publishing; 2018 [in Japanese].
[15] Bogy DB. Edge- bonded dissimilar orthogonal elastic wedges under normal and shear loading. Trans ASME, J Appl Mech 1968;35:460–6.
[16] Bogy DB. Two edge-bonded elastic wedges of different materials and wedge angles under surface tractions, trans ASME. J Appl Mech 1971;38:377–86.
[17] Sawa T. Visually passed skill test practical examination normal lamb work level 2 "procedures and explanations. Nikkan Kogyo Shimbun; 2009 [in Japanese].
[18] Suzuki Y. Adhesive tensile strengths of scarf and butt joints of steel plates (3rd report, relation between adhesive layer thicknesses and adhesive strenghs of joints). JSME Int J 1987;30(265):1042–51.
[19] Suzuki Y. Adhesive tensile strengths of scarf and butt joint of steel plates (1st report, A case of brittle adhesive). Bulletin of JSME 1984;27(233):2372–9.
[20] Murakami Y. Metal fatigue: effects of small defects and nonmetallic inclusions. Elsevier; 1993. p. 24–7.
[21] Miyazaki T, Noda NA. Evaluation of debonding strength of single lap joint by the intensity of singular stress field. J Phys Conf 2017;843(1):012006.
[22] Chen DH, Nisitani H. Mode I and II singular stress fields near a corner of jointed dissimilar materials. JSME Int J Ser. 1, Solid mech, strength of mat 1992;35(No. 4): 392–8.